Bioactive Materials 16 (2022) 218–231

Contents lists available at ScienceDirect

Bioactive Materials

journal homepage: www.keaipublishing.com/en/journals/bioactive-materials

3D-printed NIR-responsive shape memory polyurethane/magnesium scaffolds with tight-contact for robust bone regeneration

Yuanchi Zhang [a,1], Cairong Li [a,1], Wei Zhang [a,**], Junjie Deng [a], Yangyi Nie [a], Xiangfu Du [a], Ling Qin [a,d,e], Yuxiao Lai [a,b,c,e,*]

[a] Centre for Translational Medicine Research & Development, Shenzhen Institute of Advanced Technology, Chinese Academy of Sciences, Shenzhen, China
[b] University of Chinese Academy of Sciences, Shenzhen, China
[c] Key Laboratory of Health Informatics, Chinese Academy of Sciences, Shenzhen, China
[d] Musculoskeletal Research Laboratory, Department of Orthopaedics & Traumatology, The Chinese University of Hong Kong, Hong Kong SAR, China
[e] CAS-HK Joint Lab of Biomaterials, Shenzhen, China

ARTICLE INFO

Keywords:
Shape memory polyurethane
Magnesium
3D printing
Robust bone regeneration
Tight-contact

ABSTRACT

Patients with bone defects suffer from a high rate of disability and deformity. Poor contact of grafts with defective bones and insufficient osteogenic activities lead to increased loose risks and unsatisfied repair efficacy. Although self-expanding scaffolds were developed to enhance bone integration, the limitations on the high transition temperature and the unsatisfied bioactivity hindered greatly their clinical application. Herein, we report a near-infrared-responsive and tight-contacting scaffold that comprises of shape memory polyurethane (SMPU) as the thermal-responsive matrix and magnesium (Mg) as the photothermal and bioactive component, which fabricated by the low temperature rapid prototyping (LT-RP) 3D printing technology. As designed, due to synergistic effects of the components and the fabrication approach, the composite scaffold possesses a homogeneously porous structure, significantly improved mechanical properties and stable photothermal effects. The programmed scaffold can be heated to recover under near infrared irradiation in 60s. With 4 wt% Mg, the scaffold has the balanced shape fixity ratio of 93.6% and shape recovery ratio of 95.4%. The compressed composite scaffold could lift a 100 g weight under NIR light, which was more than 1700 times of its own weight. The results of the push-out tests and the finite element analysis (FEA) confirmed the tight-contacting ability of the SMPU/4 wt%Mg scaffold, which had a signficant enhancement compared to the scaffold without shape memory effects. Furthermore, The osteopromotive function of the scaffold has been demonstrated through a series of *in vitro and in vivo* studies. We envision this scaffold can be a clinically effective strategy for robust bone regeneration.

1. Introduction

Bone defect as a result of diseases and traffic accidents is one of the most detrimental medical issues due to its high disability and morbidity [1], of which the orthopedic surgery cases have been predicted globally to reach over 28 million by 2022 [2]. Conventional treatment for large bone defects is to use bone grafts harvested from the patients or compatible donors for bone fixation and regeneration, however, this common practice is still associated with several limitations, including unmatched shape, disease transmission, and additional morbidity [3–6]. Various kinds of synthetic biomaterials have been explored as bone grafts, e.g. metals, ceramics and hydrogels, however, they also encounter some drawbacks, including unsatisfied mechanical and bioactive performances [7–11]. What is more, it has been reported that poor integration between the grafts and bone tissues lead to increased loose risks and ineffective treatment [12–14]. On the contrary, an

Peer review under responsibility of KeAi Communications Co., Ltd.
* Corresponding author. Centre for Translational Medicine Research & Development, Shenzhen Institute of Advanced Technology, Chinese Academy of Sciences, Shenzhen, China.
** Corresponding author.
E-mail addresses: zhang.wei@siat.ac.cn (W. Zhang), yx.lai@siat.ac.cn (Y. Lai).
[1] These authors contributed equally to this work.

https://doi.org/10.1016/j.bioactmat.2021.12.032
Received 23 September 2021; Received in revised form 13 December 2021; Accepted 26 December 2021
Available online 31 December 2021

improved initial tight-contact and maintained bone integration of the implants could promote bone repair [15]. Hence, biomaterials enabling close integration with the defective bone are always expected. For example, injectable cements were popular owing to its fitting ability, but their mechanical properties, imporous structures, and lack satisfied cytocompatibility contribute to limited practical applications [16]. Therefore, a tight-contacting porous scaffold that could be compatible with the medical indications is highly desirable.

Shape memory polymers (SMPs), a kind of burgeoning smart materials, have captured extensive attention in the biomedical field [17–21]. SMPs have the ability to switch its shape between a programmed and an initial state under various stimuli such as heat [22,23], light [24,25], water [26,27], or magnetism [28,29]. Take the typically thermal-responsive shape memory polyurethane (SMPU) as an example, this SMPU could be deformed to a smaller shape by an external force at the temperature above its transition temperature ($T > T_{trans}$), and then fix the temporary shape at low temperature ($T < T_{trans}$); upon the temperature is higher than the transition temperature ($T > T_{trans}$), the SMPU could recover spontaneously to its original shape [30,31]. In addition to the shape memory effect, SMPs possess massive advantages including low cost, large deformation, light weight, as well as biocompatibility. Therefore, SMPs have been reported as abundant biomedical devices like actuator [32], vascular graft [33], heart scaffold [34] and artificial muscle [35]. Advances in SMPs hold considerable promises for patients with bone defects, that allow the implants to be pre-programmed to a smaller size and then recovered after being inserted so that the defective site could be well supported and fixed [36]. The shape recovery process could also strengthen the tightness of contact between the material and the surrounding tissue, improving osseointegration [8]. Also, a poly (ε-caprolactone)-based SMP scaffold with the self-fitting ability was developed for treating irregular bone defects [37]. Regrettably, the porosity of the scaffold was not controllable precisely and there was no *in vivo* study to further prove its feasibility in promoting bone regeneration. Besides lacking precise porous structures and bioactivity, most thermal responsive SMP implants have to comply with the contact actuation, which could limit clinical operation in deep area in organisms [19]. In comparison, light trigger is attractive due to its remotely controllable capability, as well as higher spatial and temporal resolution [24,38]. Particularly, near-infrared (NIR) light is widely used in biomedical application owning to its tissue harmless and excellent tissue penetration ability [39–41]. As a result, NIR-responsive SMP composites have been energetically developed through introducing different photothermal agents e.g. gold nanoparticles [42], carbon nanotubes [43], and black phosphorus nanosheets [44] into SMP matrix, resulting in light absorption and subsequent light-to-thermal energy conversion. But most photothermal agents suffer from the poor biodegradability or osteogenicity and unsatisfied mechanical properties [44], thus although a NIR-photoresponsive shape memory composite scaffold has tremendous clinical value, it remains an ongoing challenge.

Previously, our group has made great efforts on fabricating bioactive scaffolds for bone repair including integrating magnesium (Mg) particles in the polymer matrix (such as poly (lactide-co-glycolide), PLGA; poly-L-lactide, PLLA) to construct the bone scaffold by a unique 3D-printing technology [45–48]. On one hand, Mg has been widely studied in orthopedic implants on account of its comparable mechanical properties, biocompatibility, excellent biodegradability, and osteopromotive effects during degradation [49–54]. In our fundamental study, the magnesium ions (Mg^{2+}) has been proved to promote the neuronal calcitonin gene-related polypeptide-α (CGRP) -mediated osteogenesis differentiation [55]. Mg^{2+} could also regulate the metabolism of minerals and cell functions including adhesion, proliferation, and migration, as well as promote neovascularization [56,57]. Interestingly, we also found that Mg particles were promising photothermal fillers to realize local hyperthermia and has reported an Mg-containing scaffold for antitumor and bone regeneration [58]. Based on its bioactivity and photothermal property, we designed to introduce Mg particles to the SMPU matrix and then regulate its shape recovery and osteopromotive function. On the other hand, 3D-printing technology is an effective tool for constructing precise scaffold for biomedical applications, which has become an ever-increasing interest of biomedical field as well [59–61]. In particular, our group previously reported an innovative low-temperature rapid prototyping (LT-RP) 3D-printing technology that could use polymeric solution to fuse deposition and model scaffold under −30 °C followed by lyophilization to remove the solvent [62–65]. The printing process does not require reaction initiators and high temperature that might decrease the bioactivity and biocompatibility of the implants. Besides, this 3D printing technology incorporating computer-aid design could fabricate the customized composite scaffolds for bone defect repair through regulating the printing parameters e.g. temperature and/or speed of the nozzle to obtain the hierarchically macro- and micro-porous structures and controllable distribution of ingredients.

Herein, we propose a NIR-responsive and osteopromotive SMPU/Mg composite porous scaffold fabricated by the LT-RP 3D-printing technology. Based on the clinical indications, this 3D printed composite scaffold was expected to have synergistic effects to achieve the improved mechanical and bioactive properties, also be equipped with the uniform porous structure and NIR-responsive shape memory effect to enable the tight-contact for robust bone regeneration. The working concept of this 3D printed scaffold for robust bone regeneration is described as "3R" process: after being implanted, the programmed scaffold will *recovered* in presence of NIR light, achieving the tight-contact; then Mg ions will be *released* slowly with the degradation of Mg particles to promote osteogenesis; ultimately, the defective bone will be *repaired* (Fig. 1). As a proof of concept, a polycaprolactone (PCL)-based SMPU was synthesized though one-step method. Then the Mg particles were incorporated into SMPU matrix to fabricate the SMPU/Mg composite scaffold by the LT-RP 3D printing technology. After that, the scaffold was comprehensively investigated in terms of its structure, ions release, mechanical and thermal properties, shape memory effects, as well as biological performances both *in vitro* and *in vivo*. Finite element analysis (FEA) was also performed to simulate the recovery process of the 3D printed scaffold in a simplified defective bone model.

2. Materials and methods

2.1. Materials

PCL-diol (Wñ5000) was obtained from Shenzhen Esun Industrial Co., Ltd (Shenzhen, China). 4,4-methylenebis (phenylisocyanate) (MDI) was purchased from Aladdin Bio-Chem Technology (Shanghai, China). 1, 4-Butanediol (BDO) was obtained from Sigma-Aldrich (Shanghai, China). Mg particles with particle size around 50–80 μm were procured from Tangshan Wei Hao Magnesium Powder Co., Hebei, China). The PCL-diol and BDO were in advance dried under vacuum at 100 °C for 24 h to remove the moisture.

2.2. Synthesis of the SMPU matrix

The SMPU was synthesized through a one-step method. The process could be found in Fig. S1. Briefly, PCL-diol, MDI and BDO were added in a three-necked, round-bottomed flask followed by reacting at 85 °C under vacuum for 5 min with mechanical stirring. Then the solution was poured into a tetrafluoroethylene (TFE) mold, which was placed into an oven to continue the reaction for 16 h. The weight ratio of PCL-diol/MDI/BDO was 20/7/2.16.

2.3. Preparation of 3D printed scaffolds

1, 4-dioxane (Shanghai LingFeng Chemical Reagent Co., Ltd., Shanghai, China) and dimethylsulfoxide (DMSO, Aladdin Bio-Chem Technology, Shanghai, China) were mixed at a weight ratio of 5:1 to dissolve the as prepared SMPU (25%, w/v). Mg particles were added to

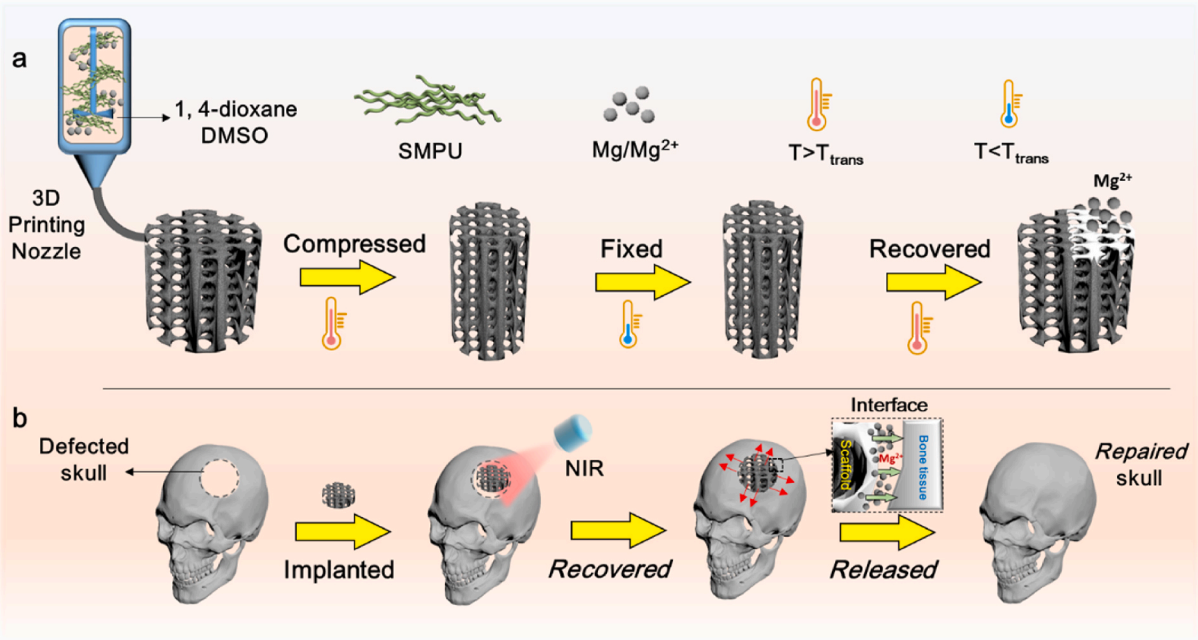

Fig. 1. Schematic illustration of: (a) 3D printed SMPU/Mg scaffold and its Mg^{2+} releasing: the scaffold could be compressed at $T > T_{trans}$ and then fixed at $T < T_{trans}$; upon $T > T_{trans,}$ the scaffold could be recovered to its original shape and then Mg^{2+} could be released with degradation of the scaffold; (b) "3R" process: after being implanted, the compressed scaffold will be *recovered* in NIR light, resulting in the supporting stimulus at interface between the scaffold and tissue; then the Mg^{2+} will be *released* slowly to improve the regeneration of defective site; at last, the defective bone will be repaired; red arrow: supporting stimulus from the shape recovery process. (For interpretation of the references to color in this figure legend, the reader is referred to the Web version of this article.)

the above SMPU solution to make the SMPU/Mg suspensions with various Mg contents (0 wt%, 2 wt%, 4 wt%, 6 wt%, 8 wt%, relative to the weight of the SMPU) that was used to prepare the bone scaffold through a low-temperature deposition 3D printing machine (CLRF-2000-II, Tsinghua University, Beijing, China), where the scanning rate was 22 mm s^{-1}, the spinneret filling rate was 0.3 mm s^{-1} and the nozzle temperature was set to 12 °C. Finally, a cubic porous scaffold was fabricated under the low temperature of −30 °C, followed by being freeze-dried to remove solvent using a vacuum lyophilizer for 48 h (Bo Yi Kang FD-1-50, China) to obtain the final products.

2.4. Characterization of 3D printed scaffolds

A Micro-CT machine (SCANCO Medical, micro-CT 100, Switzerland) was used to scan the SMPU/4 wt% Mg scaffold. The scanning parameters were: 0.5 mm aluminium, 9 μm resolution, 70 kV voltage, and 120 μA current. After the scanning, 3D reconstruction of the scaffold was realized by a CT-analyzer. The morphological characterization of 3D printed scaffolds were conducted by scanning electron microscope with Energy Dispersive Spectrometer (SEM-EDS) (ZEISS SUPRA® 55, Carl Zeiss, Germany) at an accelerating voltage of 5 kV. The wide-angle X-ray diffraction (XRD) patterns of the samples were performed using a X-ray diffractometer (D8 Advance, Bruker, Germany) using Cu Ka radiation source (1.54 Å). The scaffolds were scanned from $2\theta = 10°$ to 80°. Fourier-transform infrared (FTIR) spectra of various scaffolds were recorded by using a FTIR spectrometer (Frontier, Perkin-Elmer, USA) in the wavenumber range of 650–4000 cm^{-1} at room temperature. Thermal analysis was conducted by a differential scanning calorimetry (DSC) (Mettler Toledo, TGA/DSC1) and a TGA machine (Mettler Toledo, DSC1), respectively. The temperature ranges in these two measurements were 30–600 °C and 0–120 °C in several. The compression tests were carried by using an Instron tester (Instron Electropuls E10000, USA) at a testing rate of 1 mm min^{-1} at room temperature. Compress Modulus and stress strength were derived from the stress-strain curves to compare the mechanical properties. The degradation and Mg^{2+} releasing were investigated through placing the scaffolds specimens in a phosphate-buffered saline (PBS) solution (pH = 7.4) with a ratio of 0.1 g mL^{-1} according on ISO 10993-12, followed by putting in a thermostatic water bath bed (70 rpm, 37 °C). The extract liquids were collected each week. Then the concentrations of Mg^{2+} were measured by inductively coupled plasma mass spectrometry (ICP, Agilent 710, California, USA). The photothermal effects of the 3D printed scaffolds were investigated by using a NIR laser in air (808 nm, P = 1 W cm^{-2}) and water (808 nm, P = 2 W cm^{-2}, LWIRPD-10F, Laserwave, Beijing, China). The data of temperature changes were recorded by a NIR camera (FLIR One, FLIR Systems, Inc, Hong Kong, China). The regular and irregular shape recovery processes were performed through placing the programmed SMPU/4 wt %Mg scaffold in the NIR (808 nm, P = 1 W cm^{-2}). Shape memory effects of the scaffolds were quantificationally studied through a compression test in air, meanwhile registering changes of the height. The original height of the scaffold was noted as L_0, the maximum compressed length was L_m at 80 °C and the fixed height of the sample at the equilibrium state was L_f. After being recovered at 80 °C, the final height was L_r. Then the shape fixity ratio (R_f) and shape recovery ratio (R_r) could be calculated according to the equations [8].

$$Rf = \frac{L0 - Lm}{L0 - Lf} \times 100\% \quad (1)$$

$$Rr = \frac{Lr - Lf}{L0 - Lf} \times 100\% \quad (2)$$

Supporting ability of the scaffolds were further investigated by measuring the reovery stress of the compressed scaffolds under the NIR light. The SMPU and SMPU/4 wt%Mg scaffolds were first compressed 20% height, then being fixed and cooled down for 10 min at room temperature. After that, the scaffolds with fixed shape were irradiated by the NIR light (808 nm, 1 W cm^{-2}) and the stress were calculated from the generated force. In addition, the compressed SMPU/4 wt%Mg scaffolds were put on a 100 g weight. Then the scaffolds were irradiated by the NIR light (808 nm, 1 W cm^{-2}) and the images were recorded.

2.5. In vitro cell studies of the 3D printed scaffolds

Cell behaviors were investigated for evaluating the biological influences of the SMPU and its composite scaffolds. Mouse embryo osteoblast precursor (MC3T3-E1) cells (ATCC, Manassas, VA, USA) and Bone Mesenchymal Stem Cells (BMSCs) collected from the femur of 1 month old male Sprague Dawley (SD) rats were utilized for evaluating the cell viability, proliferation and osteogenic differentiation, respectively. At first, the scaffolds were sterilized by gamma ray (15 kGy) for 3 h. Then the samples (3 g) were immersed with a fixed mass to medium volume ratio (0.1 g mL^{-1}) in a minimum essential medium α (α-MEM, Gibco, USA) supplemented with 10% (v v^{-1}) fetal bovine serum (FBS, Gibco, USA) and 1% (v v^{-1}) penicillin/streptomycin (Gibco, USA) (30 ml in total) for 24 h at 37 °C in 5% CO_2 atmosphere for extraction according to ISO 10993-12. MC3T3-E1 cells were cultured with the samples in a 24-well culture plate with a density of 2×10^4 cells/well in an incubator under 37 °C and 5% CO_2. Using the extract liquid of the scaffolds, the Live/Dead staining assay was carried out after 3 days incubation to investigate the cell viability and the Cell Counting Kit-8 (CCK-8, Dojindo, Japan) assay was conducted after being incubated for 1, 3, 5 or 7 days to determine the cells proliferation according to the manufacturer's instructions and literature [56,66]. The Alkaline phosphatase (ALP), ALP activity and the Alizarin Red S (ARS) staining as well as quantitative polymerase chain reaction (qPCR) analysis were conducted to assess the osteogenic differentiation of the BMSCs cultured with the scaffold samples in a 24-well culture plate (2×10^4 cells/well) in the osteogenic differentiation medium (a common medium with 10 mM β-glycerol phosphate and 50 μg mL^{-1} ascorbic acid) under 37 °C and 5% CO_2. BMSCs incubated at the same conditions without samples were regarded as the blank control. The cells were stained with BCIP/NBT staining solution (Sigma-Aldrich, Shanghai, China) after being incubated 3, 7 and 14 days following the manufacturer's protocols. The ALP activity was detected with p-nitrophenyl phosphate (pNPP) (Beyotime, China) at 3, 7 and 14 days after the addition of osteogenic extracts to the BMSCs. The ALP activity was quantified by absorbance measurements at 405 nm as our previous study [56]. The mineralization of the BMSCs was identified by ARS solution (Solarbio) qualitatively after 18 days. Images were taken by an optical microscope (Nikon, Japan). The amount of calcium deposition was further investigated quantificationally according to our previous reports [56]. In addition, gene expression of osteogenic differentiation markers (Runt-related transcription factor 2 (Runx2) and osteocalcin (OST) were evaluated through qPCR after cells were cultured for 3, 7 and 14 days. The total RNA was extracted first from each sample using an AxyPrep Multisource Total RNA Miniprep Kit (Axygen, USA), followed by generating the cDNA using a Reverse Transcription Kit (Takara, Japan). The final reaction solution was totally 20 μl containing 10 μl of 2 × Power SYBR® Green PCR Master Mix, 7.4 μl nuclease free water, 1 μl of the diluted cDNA, 0.8 μl each of forward and reverse primers. And the amplification conditions were set as: 50 °C for 2 min, 95 °C for 10 min, 40 cycles of 95 °C for 15s, 60 °C for 1 min. The fluorescence signal was recorded by a SYBR Green Detection System with a LightCyclerVR480 instrument (Roche, Switzerland) followed by being converted to the numerical values. The messenger RNA (mRNA) levels of all genes were normalized using *gapdh* as internal control. The primers could be found in Table S2. Three replicates were used for each sample.

2.6. In vivo animal studies

Surgical procedure: Six-week-old male SD rats were purchased from Beijing Vital River Company (Beijing, China) and housed under standard conditions with free access to food and water for animal experimental investigations. All procedures were approved by the Animal Research Committee of Shenzhen Institutes of Advanced Technology, Chinese Academy of Sciences (SIAT-IRB-180206-YGS-LCR-A0361-01). Total 36 rats were randomly divided into three groups for investigating the histocompatibility and biomechanical property: blank group (no scaffold, only received the defects without treatment), control group (received the defects filled by the neat SMPU scaffold, no NIR light) and experimental group (received the defects filled by the SMPU/4 wt%Mg scaffold, with NIR light). The surgical process were carried out based on the literature [67]. In particular, two critical-sized calvarial defects with a diameter of 5 mm were created in each rat. The composite scaffolds with a diameter of ~6 mm were programmed to a smaller size with a diameter of ~4 mm in advance. After being implanted in the defective site, the composite scaffolds were irradiated by the NIR light (808 nm, 2 W cm^{-2}) for 60s to recover its shape and then support the defective tissues. SMPU scaffolds with a diameter of ~5 mm were inserted with no compression. The rats with these interventions were monitored and raised in cages. After reaching the predetermined time points (4, 8 and 12 weeks), the rats were sacrificed by injecting the sodium pentobarbital with a dose of 90–120 mg per kg bodyweight.

Biomechanical investigation: Defective bones with various interventions after surgery immediately and 12 weeks were respectively collected for push-out measurement. The harvested samples were first fixed on the custom clamps in an Instron tester (Instron Electropuls E10000, USA) where the cerebral surface faced up (Fig. 5b1). Then a stainless steel rod with a diameter of 4.5 mm was aligned to the center of the initial bone defect, and compressed with a rate of 1 mm min^{-1} until failure at room temperature where the peak force was recorded.

FEA: FEA was used to further investigate the stress at the interface between the 3D printed scaffold and the bone tissues by the software Abaqus 6.14 (Dassault Systèmes, France). In this study, the scaffold and defective site in the cancellous bone were simplified to a cylinder and a cuboid, where the recovery process of scaffold in the defective bone would be simulated [8]. Materials used in the FEA model were set to be isotropic, homogeneous and linearly elastic. According to the literature, properties of a cancellous bone were assumed in this study: Young's modulus: 1.5 GPa, Poisson's ratio: 0.3, CTE: 0 [68]. For the SMPU scaffold: Young's modulus: 16.8 MPa, Poisson's ratio: 0.33; For the SMPU/4 wt% Mg scaffold: Young's modulus: 23 MPa, Poisson's ratio: 0.28. No load was applied in this system and the temperature gradient was set to 25 (initial), 30, 35, 40 and 45 °C to simulate the recovery process.

Micro-CT evaluation: At each time point, the whole skull with bone defects were dissected and harvested in 4% paraformaldehyde. All samples were scanned by a Micro-CT machine (SCANCO Medical, micro-CT 100, Switzerland) to determine the 3D structure of the bone and the growth of newly grown bone tissue. The scanning parameters were: 1 mm aluminium, 9 μm resolution, 70 kV voltage, and 120 μA current. After the scanning, 3D reconstruction of the bone was realized by a CT-analyzer and the percentages of the bone volume to total bone volume (BV/TV) and the local volumatric bone mineral density (vBMD) were also determined.

Histological analysis: Hematoxylin and Eosin (H&E) (Sigma-Aldrich, Shanghai, China) staining approaches were used for histological evaluation. The dissected samples at various time points were fixed with 10% buffered formalin followed by being decalcified in 10% ethylene diamine tetraacetic acid (EDTA) dehydrated in gradient ethanol, and finally embedded with paraffin. The processed specimens were cut into sections with a thickness of 4 μm by a paraffin slicing machine (Leica RM2235, Germany). After being stained, the sections were observed by a light microscope (Olympus IX71, Japan). The surface of the section image was divided into old bone tissues (OB), new bone tissues (NB) and scaffold samples (S) according to the features of the tissues and samples including color and position. The area was analyzed using an using an image analyzer (Image-Pro 6.0, Media Cybernetics, Silver Spring, MD, USA). Then the percent of new-growth bone tissue was the ratio of area (NB) to total area (area (NB) + area (OB) + area (OB)). In addition, to further evaluate bone formation, the osteogenesis-related proteins (OCN (PA5-96529, 1:100, invitrogen) and Runx2 (PA5-86506, 1:100, invitrogen)) were detected by immunohistochemical (IHC) staining. The

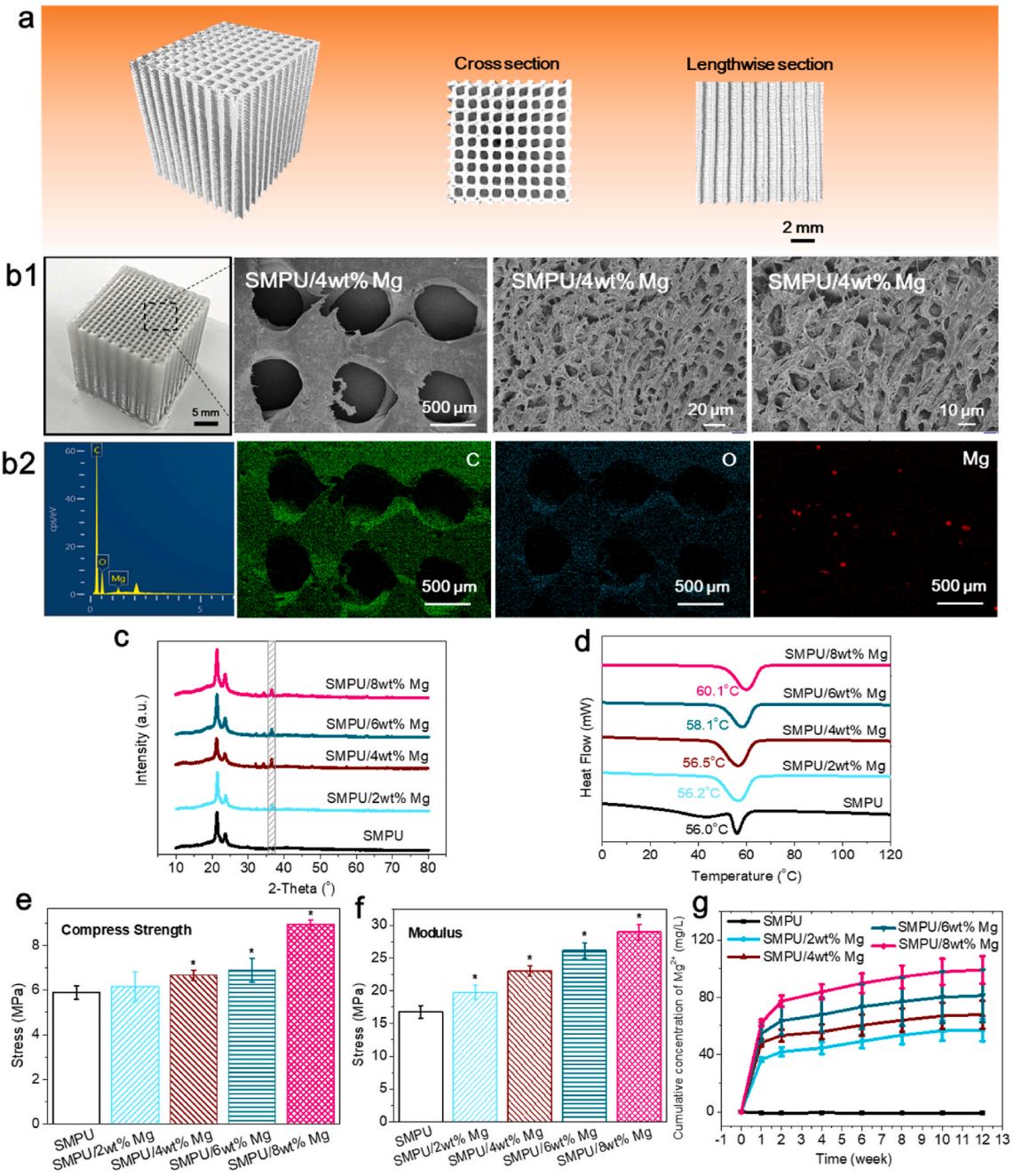

Fig. 2. Characterizations on 3D printed bone scaffolds: (a) Structural observation of SMPU/4 wt%Mg scaffold by micro-CT. (b1) Macro image and micro morphology observation with different magnification of SMPU/4 wt%Mg scaffold by SEM. From left to right at magnification of: 40x, 500x, 800x. (b2) The element composition distributed in the scaffold by SEM-EDS: Element carbon (C, green); Element Oxygen (O, blue); Element Magnesium (Mg, red). (c) XRD patterns.; (d) DSC results. (e-f) Mechanical properties: compress strength (e) and compress modulus (f) derived from the stress-stain curve. (g) Accumulated concentration of released Mg^{2+}. n = 3. *, significant difference compared to the SMPU group, $p < 0.05$. (For interpretation of the references to color in this figure legend, the reader is referred to the Web version of this article.)

Goldner's trichrome (Sigma, USA) staining was also carried out according to previous studies [56].

2.7. Statistical analysis

Quantitative results were analyzed using the software SPSS 17.0. The graphics of the data analysis were prepared though the software Origin 8.5. The statistical significance among different groups or time points was calculated using one-way or two-way ANOVA analysis and the significant difference was set to $p < 0.05$.

3. Results

3.1. Characterization on 3D printed SMPU/Mg scaffolds

The PCL-based SMPU matrix was firstly synthesized through a one-step method (Fig. S1). Then through the unique LT-RP 3D printing technology, the SMPU/Mg composite scaffolds with various contents of Mg particles (0 wt%, 2 wt%, 4 wt%, 6 wt%, 8 wt%, relative to the weight of the SMPU matrix) were fabricated. The reconstructed micro-CT images of the representative SMPU/4 wt%Mg scaffold presented an interconnected porous structure both horizontally and vertically

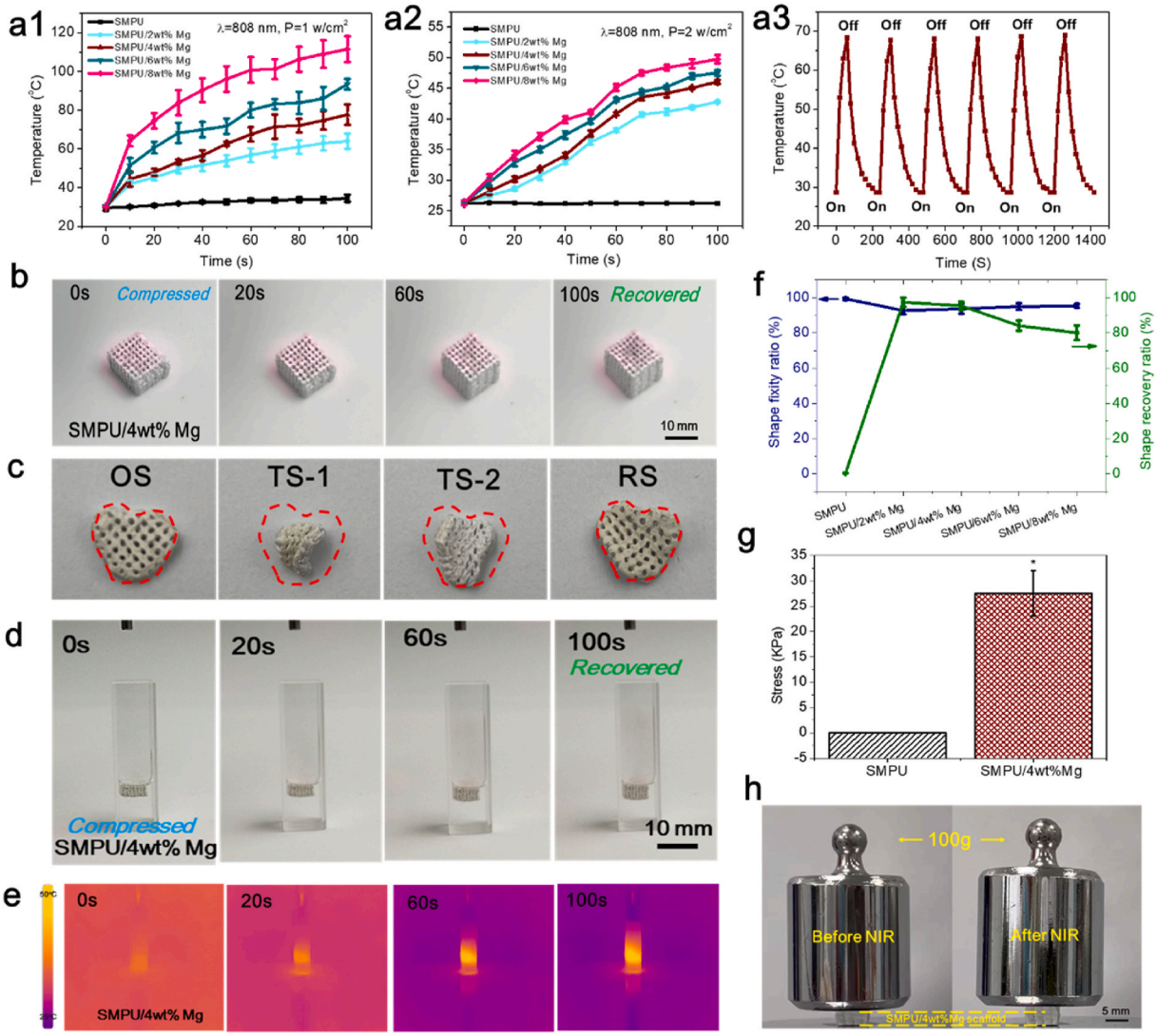

Fig. 3. Photothermal performances and shape memory effect of 3D printed scaffolds under NIR light. (a1-a2) Photothermal heating curves of the SMPU/Mg scaffolds with different Mg concentrations at dry state (a1) and wet state (a2) irradiated by the NIR laser. (a3) Temperature elevation of the SMPU/4 wt%Mg scaffold for six laser on/off cycles. (b–c) Photographs of shape recovery process in air of the regular (b) and irregular (c) SMPU/4 wt% Mg scaffold irradiated by the 808 nm laser (1 W cm^{-2}). OS: original shape; TS-1: Temporary shape-1; TS-2: Temporary shape-2; RS: recovered shape. (d) hotographs of shape recovery process in water of the SMPU/4 wt%Mg irradiated by the 808 nm laser (2 W cm^{-2}). (e) Infrared thermal images of the recovery process in water. (f) R_f and R_r of the SMPU/Mg scaffolds with different Mg concentrations. (g) Recovery stress of SMPU and SMPU/4 wt% Mg scaffold irradiated by the 808 nm laser (1 W cm^{-2}). (h) Programmed SMPU/4 wt% Mg scaffold compressed with a 100 g weight before and after being irradiated by the 808 nm laser (1 W cm^{-2}). n = 3.

observed from the views of its cross section and lengthwise section (Fig. 2a). The pristine SMPU presents a white color (Fig. S2), and the color becomes darker in the SMPU/4 wt%Mg scaffold (Fig. 2b1). SEM images reveal the hierarchical porous structure in the scaffolds that have the macropores with 600–700 μm diameters (Table S1 and Fig. S3a) and the micropores with the diameters of 5–40 μm (Fig. 2b1). In addition, the samples were also observed by SEM-EDS and identified that Mg particles are homogeneously distributed in the scaffolds (Fig. 2b2). The FTIR spectrum proves that the NCO- groups in SMPU and SMPU/Mg composites was reacted completely, which the SMPU matrix has been prepared well (Fig. S3b). Due to the existence of Mg particles, the typical peaks of appear at $2\theta = 36.7°$ in the corresponding XRD patterns of the composite scaffolds while no peak is in that of the pristine SMPU (Fig. 2c). The differential thermogravimetry (DTG) thermograms of the 3D printed scaffolds from the thermogravimetric analysis (TGA) curve were shown in Fig. S4. The initial and maximum decomposition temperature of the neat SMPU sample was 316.5 °C and 367 °C while those of the Mg-containing samples decreased to 304.8/344.6 °C of SMPU/4 wt%Mg and 298.6/332.7 °C of SMPU/8 wt%Mg. The melting temperature (T_m) of the samples were measured by DSC. As shown in Fig. 2d, compared with the pristine SMPU ($T_m = 56.0$ °C), the T_m increased after adding the Mg particles in the composite, which had a positive relationship between the T_m and the Mg content. Fig. 2e and f shows the strength and modulus of the scaffolds at room temperature derived from the typical stress−strain curves (Fig. S5). The pristine SMPU has a compress strength of ~5.9 MPa and a modulus of ~16.8 MPa. After introducing the Mg particles, the mechanical performances of the composite scaffold were enhanced with the increase of the Mg contents. For example, the strength and modulus of SMPU/4 wt%Mg sample were 6.7 MPa and 23.0 MPa in several, which have significant improvements compared with those of the neat SMPU. The *in vitro* degradation of the scaffolds was investigated through immersing them in phosphate-buffered saline (PBS) solution (pH = 7.4) for 12 weeks. After 12 weeks, the weight of the samples had no significant changes (Fig. S6a), suggesting the stability of the scaffolds. The accumulative Mg^{2+} releasing curve (Fig. 2g) was derived from to the concentration of

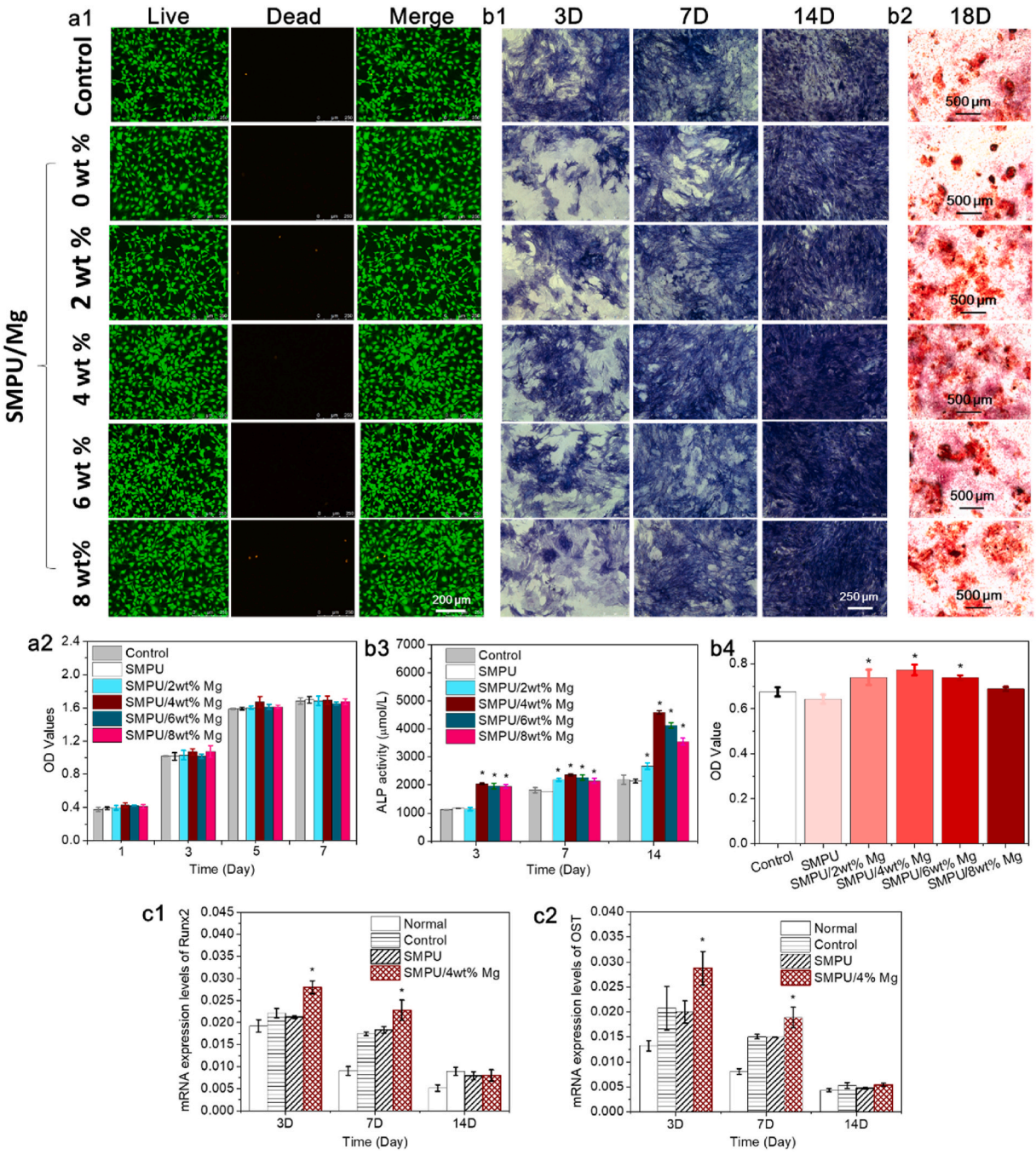

Fig. 4. *In vitro* cell studies of the 3D printed scaffolds. (a1) Fluorescence images of MC3T3-E1 cells after 3 days incubation, where the live cells are in green and dead cells are in red. (a2) Cell proliferation of MC3T3-E1 cells. Osteogenic differentiation: (b1) ALP staining of BMSCs at 3, 7 and 14 days. (b2) ARS staining of BMSCs at 18 days. (b3) ALP activity. (b4) Quantitative analysis of calcium nodules. (c1-c2) Expression levels of Runx2 (c1) and OST (c2) of rat BMSCs at 3, 7 and 14 days. n = 3. *, significant difference compared to the normal, control and SMPU groups, $p < 0.05$. (For interpretation of the references to color in this figure legend, the reader is referred to the Web version of this article.)

released Mg^{2+} at each time point of the various extracts (Fig. S6b). Compared to the pure SMPU scaffold presenting no Mg^{2+} releasing, the SMPU/Mg composite scaffolds released Mg^{2+} rapidly in first 2 weeks. From 2 to 12 weeks, the Mg^{2+} releasing speed leveled off gradually. The results demonstrated the sustainable release of the Mg^{2+} from the 3D printed composite scaffolds.

3.2. Photothermal performances and shape memory effect of the 3D printed scaffolds

The NIR photothermal effects of the scaffolds at dry state and wet state were investigated by irradiating the samples using an 808 nm laser where the power density was set to 1 w cm^{-2} and 2 w cm^{-2}, respectively. As shown in Fig. 3a1, the increased temperatures of the scaffolds at dry state were observed with increases of Mg concentration and irradiating time, and had a higher ramp rate during first 60 s. Specifically, SMPU/4 wt%Mg scaffold presented a temperature rise from ~30.0 °C to ~67.6 °C (higher than its T_m) in 60s and finally achieved ~77.7 °C after being heated for 100s (P = 1 w cm^{-2}). On the contrary, the temperature of pure SMPU scaffold had almost no change after the same irradiating operation. The photothermal effects of the scaffolds at wet state had the same trend with that at dry state (Fig. 3a2). Even

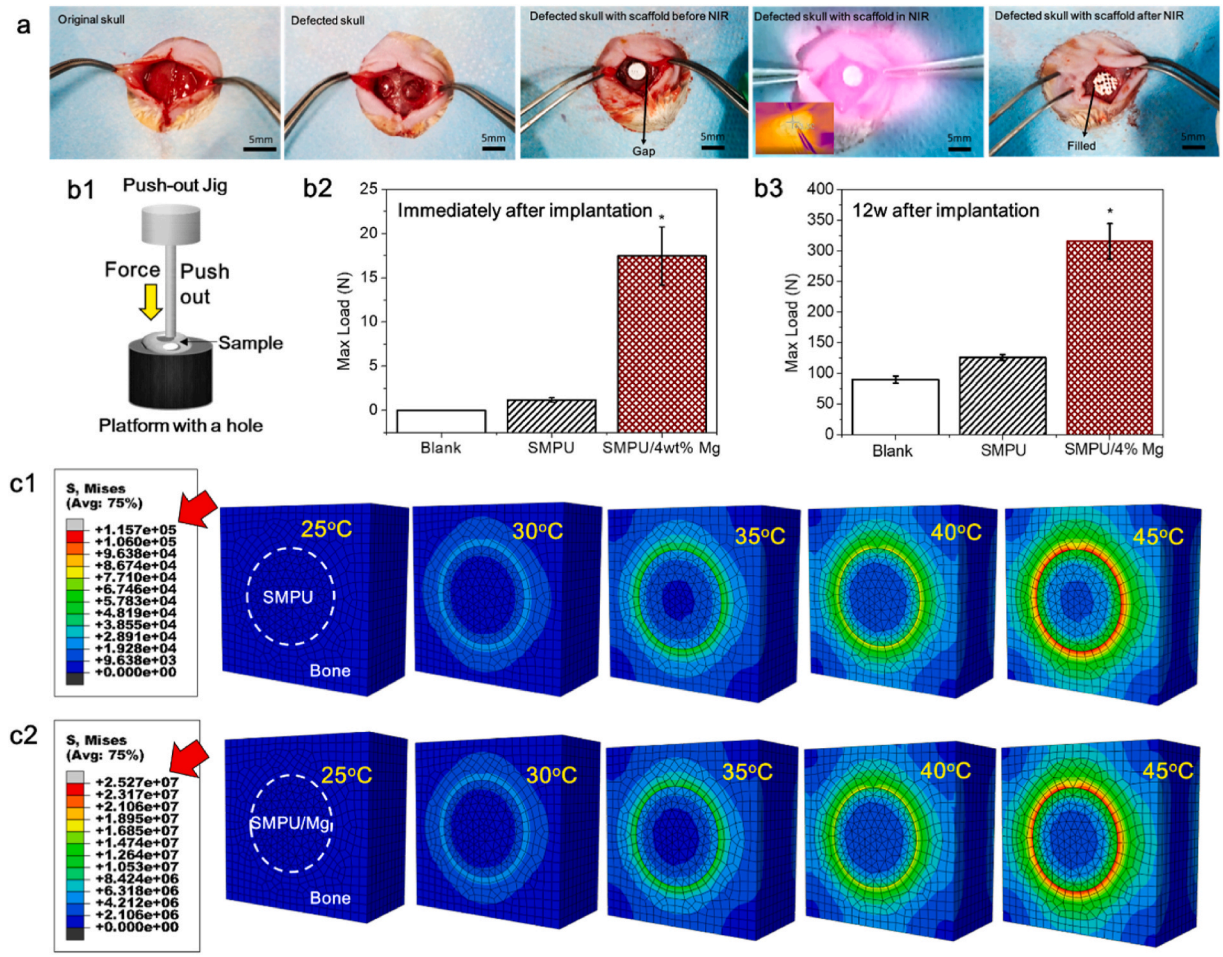

Fig. 5. Implantation of the 3D printed scaffolds at the defective sites. (a) The shape recovery process of the scaffold during implanting process. (b1) Schematic illustration of a push-out jig. (b2) Pull-out test results after implantation immediately. (b3) Pull-out test results after implantation for 12 weeks. (c1-c2) Equivalent stress distribution by FEA during the recovery process of the pristine SMPU (c1) and SMPU/4 wt% Mg scaffolds (c2) in the defect site. Red arrow: the highest von Mises stresses. n = 3. *, compared to the blank and SMPU scaffold groups, significant difference, $p < 0.05$. (For interpretation of the references to color in this figure legend, the reader is referred to the Web version of this article.)

through there was the fast heat dissipation in water, the samples could still realize the local hyperthermia when the power was set to P = 2 w cm^{-2}. For example, the temperature of the SMPU/4 wt%Mg scaffold rose from ~26.2 °C to ~40.8 °C in 60s and finally was ~46.1 °C. For further evaluating the photothermal stability of the SMPU/4 wt%Mg scaffold, the temperature changes of the scaffold exposed in the NIR light for 60 s (laser on) was recorded, followed by natural cooling to room temperature after the NIR laser was turned off (laser off). Even the cycles repeated 6 times, the efficiency of the photothermal effects had little decay, which proved the excellent photothermal stability of the SMPU/4 wt%Mg scaffold (Fig. 3a3).

Shape memory properties of the scaffolds through remote NIR light trigger were investigated. The scaffold was compressed at $T > T_m$, and then cooled down to room temperature until the shape was fixed. After that, the compressed scaffold was placed under the NIR light with an 808 nm laser (P = 1 W cm^{-2}). With exporue of the NIR light over time, the shape of the scaffold could be recovered spontaneously to the original state (Fig. 3b). In Fig. 3c, the SMPU/4 wt%Mg scaffold was customized to an irregular shape and the results also confirmed the recovery effects of the SMPU/4 wt%Mg scaffold. In Fig. 3d, the compressed scaffold was immersed into water, where the shape of the scaffold could still be recovered to the initial state in 100s under the NIR light (808 nm, 2 W cm^{-2}). Fig. 3e presents the infrared thermal images of the recovery process. To quantify the shape memory properties of the scaffolds, the variation of the height were recorded and then measured (Fig. 3f). After being irradiated for 100s, the pristine SMPU had a ~99.3% of shape fixity ratio (R_f) while a ~0.5% of shape recovery ratio (R_r) due to no photothermal effect. Interestingly, R_f of the Mg-containing scaffolds decreased while R_r increased with the increasing concentration of Mg particles. For instance, the R_f and R_r of SMPU/2 wt%Mg were ~92.8% and ~97.4%, respectively. For SMPU/8 wt%Mg, the corresponding ratios became ~95.4% and ~80.0% in several. For obtaining a balanced shape memory performance, this work selected the SMPU/4 wt %Mg scaffold (93.6% of R_f and 95.4% of R_r) to process the following animal studies. The supporting ability of the SMPU/4 wt%Mg scaffold was also evaluated. Fig. 3g displays the recovery stress of the pure SMPU and SMPU/4 wt%Mg scaffold under NIR light. Due to no NIR-responsive effect, the SMPU scaffold had no recovery stress. In contrast, the SMPU/4 wt%Mg scaffold had a recovery stress of ~27.5 KPa. In addition, because of the recovery effect, the scaffold could lift a 100 g weight in the presence of NIR light, which was more than 1700 times of its own weight (Fig. 3h). These results proved that the 3D printed SMPU/Mg scaffolds had good NIR-responsive properties and supporting ability, stemming from their excellent photothermal effects of Mg particles and the thermo-responsivity of the SMPU.

3.3. *In vitro cell studies of the 3D printed scaffolds*

MC3T3-E1 cells were used to evaluate the effects of the 3D printed scaffolds on cell viability and proliferation while the control group had

no additional treatment. Fig. 4a1 shows the fluorescence images of MC3T3-E1 cells incubated with various samples for 3 days through the Live/Dead staining assay. Cells could be found clearly with an obviously high viability of for all groups. In addition, the quantitative results of the cell proliferation cultured with SMPU and its composite scaffolds for 1, 3, 5 and 7 days were shown in Fig. 4a2, which indicated the MC3T3-E1 cells proliferated more along with time in all groups. After 5 days, the speed of the cell proliferation decreased and there was no obvious increase at 7 days. In addition, there was also no significant difference among various groups in terms of the OD values.

The effects of the scaffolds on osteogenic differentiation were also investigated using the BMSCs [69]. The ALP staining results at the time points of 3 days, 7 days and 14 days (Fig. 4b1) indicated that the purple ALP-staining colony increased over time, which suggested the continuous ALP secretion due to osteogenic differentiation of the BMSCs. At 3 days, the purple color in stained colony of the control group was darker than that of the scaffolds groups, meaning the control group (without any scaffold) had the best osteogenic differentiation. After 7 days, the stained colony of the scaffolds groups was darker. Moreover, the purple color was darker with the increasing content of the Mg particles due to enhanced bioactivity of the released Mg^{2+}. The ALP activity suggested that the Mg-containg composite groups, especially the SMPU/4 wt%Mg group had significant higher ALP activity compared with that in the control and SMPU groups (Fig. 4b3). The ALP activity decreased in the SMPU/6 wt%Mg and SMPU/8 wt%Mg groups after 14 days incubation. Furthermore, the qualitative and quantitative analysis of the calcium nodules during the BMSCs incubation with various samples were also evaluated through the ARS staining method. As shown in Fig. 4b2, the red mineralized nodules indicated that calcium deposited successfully after 18 days incubation. Compared with the control group and the pure SMPU group, the calcium nodules were improved after introducing Mg particles. However, the mineralized nodules decreased in the SMPU/8 wt%Mg group. The same trend was confirmed by the quantitative analysis in Fig. 4b4. The quantified optical densities of alizarin red in SMPU/2 wt%Mg, SMPU/4 wt%Mg group and SMPU/6 wt%Mg groups were significantly higher than those in the control group and the pure SMPU group while the data decreased obviously in the SMPU/8 wt%Mg group. Even though there was a dosage effect, the 3D printed SMPU/Mg scaffolds were proved to enhance osteogenic differentiation of BMSCs. The normal groups (without osteogenic induction medium) of the ALP staining assay and the ARS staining assay could be found in Fig. S7. The gene expression of the Runx2 and OST of the BMSCs incubated after 3 days, 7 days and 14 days were determined by qPCR. Compared with the normal group (without osteogenic differentiation medium and scaffold), the control group (without any scaffold), and the neat SMPU group, SMPU/4%Mg group has a significant improvement at early stage (3 days and 7 days) expressing the highest level of Runx2 and OST (Fig. 4c1 and 4c2) [56,70]. Primer sequences of Runx2 and OST for qPCR could be found in Table S2. This result also confirmed the osteopromotive effects of the SMPU/4%Mg scaffold that was used for the further *in vivo* studies.

3.4. *In vivo animal studies*

The *in vivo* bone regenerative potential of the 3D printed scaffold was evaluated systematically. At first, shape memory behavior of the SMPU/4 wt%Mg scaffold during the implanting process could be found in Fig. 5a. The calvarial defect of the mouse was created, followed by being filled with the compressed SMPU/4 wt%Mg scaffold. Due to the programmed small size, there was a gap between the scaffold and the bone tissue so that the scaffold could be easily implanted in the defective site. Subsequently, the defective skull with the composite scaffold was irradiated by the NIR light (808 nm, 2 W cm^{-2}) for 60s, and finally the scaffold recovered to its original size with its porous structure.

The push-out tests were conducted to investigate the tight-contacting performance of the scaffolds and the biomechanical properties of the repaired defects (Fig. 5b2 and 5b3). After implantation immediately, the blank group (no implantation) has no any loading ability. For the pure SMPU scaffold group, the maximum load was ~1.2 N due to the presence of the scaffold. For SMPU/4 wt%Mg scaffold group, the peak force had a significant enhancement to ~17.5 N. At 12 weeks implantation, the blank group had new growth tissues with a maximum load of ~90 N. As for the SMPU/4 wt%Mg scaffold group, the maximum load of the defective samples was significantly enhanced from ~126 N (in SMPU scaffold group) to ~316 N. This might be caused by the improved newly growth bone tissues resulted from the tight-contact of the composite scaffold and the releasing of the Mg^{2+}. In order to analysis the tight-contacting ability of the 3D printed scaffold after implantation immediately, FEA method was performed. The implanted bone site was simplified to a defective bone-scaffold mode as shown in Fig. 5c1 and 5c2, where the scaffold was regarded as a compressed shape. The pristine SMPU scaffold had a R_r of 0.05% due to no photothermal effects while the SMPU/4 wt%Mg scaffold had a R_r of 95.4%. To focus on the effect of the shape recovery process, we here only consider the shape memory properties of the scaffold rather than its thermal expansion performances. Therefore, the coefficient of thermal expansion (CTE) in the system would be modified as the parameter. The original CTE equation was shown here [71].

$$\alpha = \Delta L / L \Delta T \tag{3}$$

Where ΔL is the elongation of the sample; L is the original length of the sample; ΔT is the difference in temperatures before and after expanding.

In this study, due to the shape memory effects, based on equations (1) and (2) in the **Experimental section,** the new-modified CTE equation was regarded as below:

$$\alpha = \frac{Lr - Lf}{Lf \Delta T} = Rr\left(\frac{L0}{Lf} - 1\right) * \frac{1}{\Delta T} \tag{4}$$

Where the original height of the scaffold was noted as L_0, the fixed height of the sample at the equilibrium state was L_f. After being recovered, the final height was L_r.

As a result, if the L_0 and L_f was fixed, there is a proportional relation between CTE and the shape recovery properties of the sample. According to this equation (4), in this study, the temperature range is 20 °C, and the new-modified CET values for filling in the system were 0.00005 for the pristine SMPU scaffold and 0.00954 for the SMPU/4 wt%Mg scaffold. In the stress nephograms, with temperature rising, the stresses appeared and increased due to the shape recovery process of the scaffolds and the highest von Mises stresses existed at the interface. Specifically, the pure SMPU scaffold had only ~115.7 KPa of the highest von Mises stresses while the SMPU/4 wt%Mg scaffold had ~25.27 MPa of the highest von Mises stresses, which caused by the shape recovery process. These also confirmed the tight-contact of the 3D printed SMPU/Mg scaffold.

Micro-CT analysis was used to investigate the newly grown bone tissues at 4, 8 and 12 weeks after surgery. The 3D reconstruction image by micro-CT shown in Fig. 6a1. Compared to the blank group (without any scaffold) and the pristine SMPU scaffold group, the calvarial defect filled by SMPU/4%Mg scaffold had more newly regenerated bone at each time point, especially at 12 weeks. For quantitative analysis, the percentages of the bone volume to total bone volume (BV/TV) and the local volumatric bone mineral density (vBMD) were calculated (Fig. 6a2 and 6a3). The data in SMPU scaffold group has an improvement compared with that in the blank group at each time-point, which might imply the scaffolds with hierarchically macro- and micro-porous structures could enhance bone regeneration. As for the SMPU/4%Mg scaffold group, both the vBMD and BV/TV had a significant enhancement than those in the blank and SMPU groups at 4, 8 and 12 weeks after implantation. For instance, the vBMD and BV/TV of the composite scaffold group were respectively ~0.76 and 19.8% at 12 weeks while those in the SMPU scaffold group were 0.54 and 15.9%, and in the blank group were only 0.41 and 11.5%. In addition, quantitative analysis of the trabecular

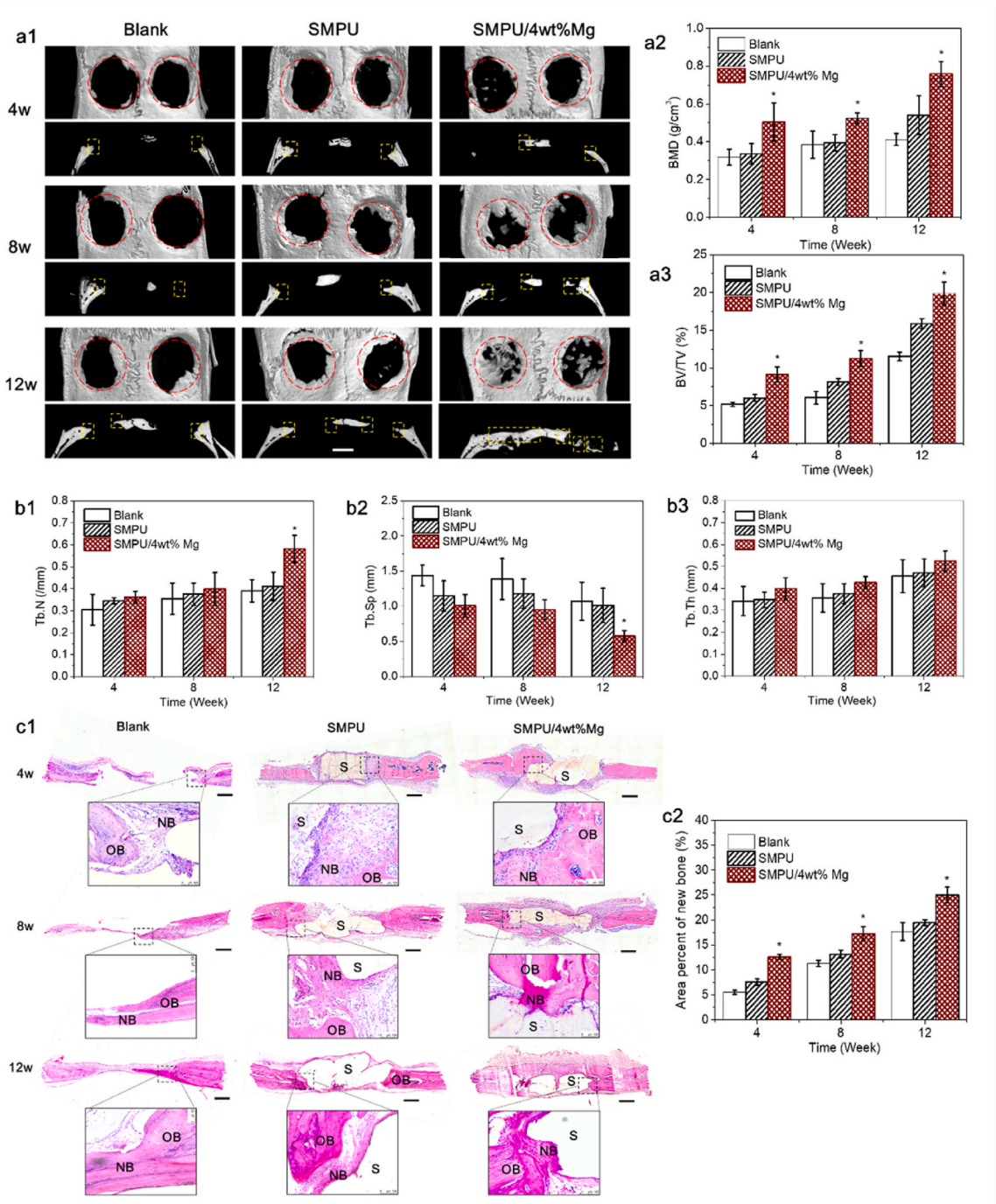

Fig. 6. *In vivo* animal studies. (a1) Micro-CT 3D reconstruction of defective bones and their sagittal images at 4, 8, 12 weeks. Red circle: defective area. Yellow frame: new bone tissues. The scale bars are 2 mm. (a2) BMD and (a3) BV/TV varied in each group at 4, 8, 12 weeks. (b1-b3) Quantitative analysis of the trabecular number (b1), trabecular separation (b2), and trabecular thickness (b3). (c1) Histological sections and magnified views of the defective site with or without the scaffolds after implantation for 4, 8 and 12 weeks stained with HE; OB: old bone tissues, NB: new bone tissues; S: scaffold samples. The scale bar = 500 μm. (c2) Area percent of the new bone in defective sites. n = 3. *, compared to the blank and SMPU scaffold groups, significant difference, $p < 0.05$. (For interpretation of the references to color in this figure legend, the reader is referred to the Web version of this article.)

number (Tb. N), trabecular separation (Tb. Sp), and trabecular thickness (Tb. Th) (Fig. 6b1-b3) confirmed the improvement in the SMPU/4%Mg scaffold group compared with the blank and SMPU groups. The results of the representative histological H&E staining in Fig. 6c1 and 6c2 indicate the newly fomred bone tissues in each group at various time-points. Compared with the blank group and the pristine SMPU group, more new bone tissues could be found in the SMPU/4 wt%Mg group at each time point (Fig. 6c1). In addition, the new bone could also be found to be formed in the pores of the scaffolds especially in the Mg-containing scaffold explained by known osteopromotive effects of Mg^{2+}. The quantitative percentage area of the new bone tissues in the defective site also confirmed the results (Fig. 6c2). Compared to the other groups, the SMPU/4 wt%Mg group had significantly larger area of the new bone tissues after implantation 4, 8, and 12 weeks. The IHC staining and Goldner's trichrome staining results presented that the SMPU/Mg groups had higher expression of the OCN and Runx2, and more new

tissues compared with the blank and SMPU groups, respectively (Fig. S8).

4. Discussion

Existing clinical grafts are usually limited by poor contact and insufficient osteogenic activities and SMP scaffolds possess enhanced bone integration but hindered by unsuitable transition temperature and unsatisfied bioactivity for practical application. Therefore, this study provides 3D printed near-infrared-responsive and tight-contacting SMPU/Mg composite scaffolds and proves its improved mechanical properties, stable photothermal effects and osteopromotive performances. At first, the hierarchically macro- and micro-porous structures of the 3D printed scaffolds are presented (Fig. 2a and b1). Additionally, The results of the SEM-EDS (Fig. 2b2), FTIR spectrum (Fig. S3b) and XRD patterns (Fig. 2c) confirm the uniform dispersion of Mg particles and the homogenous structure of the 3D printed scaffolds [72,73]. TGA results (Fig. S4) show the thermal degradation of the SMPU and its composite scaffolds occurs in a two-step process and the Mg-containing scaffolds have a good thermal stability [74]. The transition temperature of SMPU for shape programing is usually the glass transition temperature or the melting temperature of the polyhydric alcohols. In this work, the melting temperature of the PCL part was the transition temperature, because in designed structure of the SMPU and its composites, the crystal-melt transition of PCL brings significant changes to overall property like modulus, and directly decides the shape memory performance. The DSC curves (Fig. 2d) show that the transition temperature (T_m) could increase with the increasing inorganic Mg particles and it also implies the enhanced mechanical properties that is confirmed by the compression tests (Fig. 2e and f). The SMPU and its composites could maintain stable at less three months due to its stable structure, which was expected to support mechanically the defective tissue in a long period [8]. In addition, the SMPU could be modified to biodegradable by copolymerized or grafted biodegradable block such as PCL, which could be hydrolyzed in the biological environment and finally contribute to the biodegradation of the SMPU [75]. The accumulative Mg^{2+} releasing curve (Fig. 2g) presents a rapid and stable releasing process because water molecules could easily contact to the Mg particles exposed out of surface of the SMPU/Mg scaffold, then the degradation of the Mg particles enfolded in SMPU becomes slow and stable.

Photothermal performances and shape memory effects are important in this study because they decide the responsive and tight-contacting ability of the scaffolds *in vivo*. The experimental results demonstrated that the introduction of Mg particles endowed the SMPU/4 wt%Mg composite scaffolds with stable NIR photothermal effects and enable a fast temperature increase over the T_m of the composites. According to the literature, the achieved temperature in 60 s of the composite scaffold is safe for *in vivo* study [76]. Compared to SMPU and other composite scaffolds, the SMPU/4 wt%Mg scaffold has a balanced shape memory performances (Fig. 3f). For the opposite influence of the increasing Mg particles on the R_f and R_r, on one hand, the improvement of R_f may be ascribed to the increased glassy state modulus since the shape was fixed in the glassy state. On the other hand, the decrease of the R_r may be attributed to the negative effects of Mg particles on the flexibility of the polymer chains [5]. A high R_f means a shape memory implant could be compressed to a very small size and a high R_r represents that the shape memory implant could support tightly in body [8]. In addition, the SMPU/4 wt%Mg scaffold can recover at both dry state and wet state under the NIR light, which suggests its shape memory ability could be applied in the physiological environments. The stress relaxation curve of the SMPU/4 wt%Mg scaffold (Fig. S9) show that after being placed at 37 °C for near 10 h, the composite scaffold could still offer a stress of ~23.5 KPa, which maintained the self-tight contact function. With tight contact and osteogenesis enhanced by Mg incorporated scaffold, bone ingrowth into the scaffold, which can result in good integration with the tissues.

In vitro cell studies prove that the 3D printed scaffolds have good cell biocompatibility (Fig. 4a). Although the analysis of the calcium nodules imply that the excessive Mg content has a negative influence on osteogenic differentiation [77,78], the composite scaffolds excluding SMPU/8 wt%Mg are still proved to promote effectively the osteogenic differentiation of BMSCs (Fig. 4b). In addition, the gene expression of the Runx2 and OST of the BMSCs (Fig. 4c) confirms the positive bioactivity of the SMPU/4 wt% Mg scaffold that are selected for *in vivo* studies. At first, the push-out tests demonstrates the shape recovery process can give the composite scaffold the tight-contacting ability upon being put under the NIR light. After 12 weeks implantation, the SMPU/4 wt%Mg scaffold is proved to have a good ability to contact tightly the defective site and enhanced biomechanical properties for robust bone regeneration (Fig. 5b). In this work, FEA demonstrates the stress at the interface between the scaffolds and the defective bone tissues. The FEA results confirm that the SMPU/4 wt%Mg scaffold has much better supporting ability than that of the pure SMPU scaffold (Fig. 5c). Furthermore, Micro-CT and histological staining analysis suggest the defective bone sites in SMPU/4 wt%Mg scaffold group have promoted bone regeneration than those in blank group and the pristine SMPU group, which might be caused by the bioactive effects of released Mg^{2+} from the tight-contacting scaffold [8]. Collectively, the hierarchically macro- and micro-porous structures from the 3D printing technology, the tight-contacting ability from the shape memory effects under the NIR light, and the osteogenic activities of the Mg particles guarantee the SMPU/Mg scaffolds with robust bone regeneration for potential clinical applications.

5. Conclusion

In summary, the 3D printed scaffolds made of SMPU/Mg composites with osteopromotive, NIR-responsive and tight-contacting abilities were developed in this work for addressing the limitations on low porosity, responsive temperature, unsatisfied mechanical and bioactive performances in conventional shape memory implants. First of all, the SMPU/4 wt%Mg scaffold had a hierarchical porous structure through the LT-RP 3D printing method. In addition, the scaffold had a significant enhanced mechanical properties (a compress strength of ~6.7 MPa and a modulus of ~23.0 MPa) compared to the pristine SMPU scaffold (a compress strength of ~5.9 MPa and a modulus of ~16.8 MPa). The NIR-responsive shape memory effect was realized in the composite scaffold due to the photothermal effects of Mg particles and the thermo-responsivity of the SMPU, by which the temperature could be quickly elevated under NIR light to $T > T_m$ rather than the contact actuation. High shape memory ratios lead to the programmability and supporting ability in defective site, in this work, R_f and R_r could be balanced in the SMPU/4 wt%Mg scaffold with a R_f of 93.6% and a R_r of 95.4%. The scaffold could lift the object more than 1700 times its own weight due to its shape recovery under NIR light. Furthermore, the composite scaffold was proved to support the cell survival, proliferation and osteogenic differentiation *in vitro* cell experiments. More importantly, the animal studies demonstrated the tight-contacting and osteopromotive functions of the 3D printed composite scaffold. FEA results revealed the relationship between the tight-contact and the shape recovery process, confirming the tight-contacting ability of the SMPU/4%Mg scaffold under NIR light. As described, this SMPU/Mg composite scaffold took advantages of its components (SMPU and Mg) and the LT-RP 3D printing technology to achieve the synergistic effects for the final robust bone regeneration. We envision this 3D printed bone scaffold hold great promise to be translated into clinic for robust bone regeneration.

Declaration of competing interest

The authors declare no conflict of interest.

CRediT authorship contribution statement

Yuanchi Zhang: Conceptualization, Methodology, Investigation, Visualization, Writing – original draft, Writing – review & editing. **Cairong Li:** Methodology, Investigation, Visualization, Writing – original draft, Writing – review & editing. **Wei Zhang:** Conceptualization, Methodology, Writing – review & editing. **Junjie Deng:** Investigation. **Yangyi Nie:** Investigation. **Xiangfu Du:** Investigation. **Ling Qin:** Methodology, Supervision, Writing – review & editing. **Yuxiao Lai:** Conceptualization, Methodology, Writing – review & editing, Supervision.

Acknowledgements

YC.Z. and CR.L. contributed equally to this work. This work was supported by National Key R&D Program of China (2021YFE0202600), National Natural Science Foundation of China (82022045, 81871767 and 22007098), CAS Interdisciplinary Innovation Team(JCTD-2020-19), Shenzhen Double Chain Project for Innovation and Development Industry supported by the Bureau of Industry and Information Technology of Shenzhen (201908141541), Key Filed R&D Program of Guangdong Province (2019B010941001), Key Laboratory of Health Informatics, Chinese Academy of Sciences, Shenzhen Fundamental Research Foundation (JCYJ20190807154807663, JCYJ20170818160707101), CAS-HK Joint Lab of Biomaterials, Natural Science Foundation of Guangdong Province (2018A030310670), and Natural Science Foundation of Guangdong Province (2018A030310670), Shenzhen Engineering Research Center for Medical Bioactive Materials (XMHT20190106001), China Postdoctoral Science Foundation (2020TQ0338), Special Research Assistant Project of CAS.

Appendix A. Supplementary data

Supplementary data to this article can be found online at https://doi.org/10.1016/j.bioactmat.2021.12.032.

References

[1] L. Xu, H. Qin, J. Tan, Z. Cheng, X. Luo, H. Tan, W. Huang, Clinical study of 3D printed personalized prosthesis in the treatment of bone defect after pelvic tumor resection, Journal of Orthopaedic Translation 29 (2021) 163–169, https://doi.org/10.1016/j.jot.2021.05.007.

[2] M.N. Collins, G. Ren, K. Young, S. Pina, R.L. Reis, J.M. Oliveira, Scaffold fabrication technologies and structure/function properties in bone tissue engineering, Adv. Funct. Mater. (2020) 2010609, https://doi.org/10.1002/adfm.202010609, n/a(n/a).

[3] S. Yao, X. Lin, Y. Xu, Y. Chen, P. Qiu, C. Shao, B. Jin, Z. Mu, N.A. Sommerdijk, R. Tang, Osteoporotic bone recovery by a highly bone-inductive calcium phosphate polymer-induced liquid-precursor, Adv. Sci. 6 (19) (2019) 1900683, https://doi.org/10.1002/advs.201900683.

[4] G.L. Koons, M. Diba, A.G. Mikos, Materials design for bone-tissue engineering, Nat. Rev. Mater. 5 (8) (2020) 584–603, https://doi.org/10.1038/s41578-020-0204-2.

[5] Y. Zhang, J. Hu, X. Zhao, R. Xie, T. Qin, F. Ji, Mechanically robust shape memory polyurethane nanocomposites for minimally invasive bone repair, ACS Applied Bio Materials 2 (3) (2019) 1056–1065, https://doi.org/10.1021/acsabm.8b00655.

[6] G. Xu, X. Hu, L. Han, Y. Zhao, Z. Li, The construction of a novel xenograft bovine bone scaffold, (DSS)6-liposome/CKIP-1 siRNA/calcine bone and its osteogenesis evaluation on skull defect in rats, Journal of Orthopaedic Translation 28 (2021) 74–82, https://doi.org/10.1016/j.jot.2021.02.001.

[7] W. Zhao, Z. Huang, L. Liu, W. Wang, J. Leng, Y. Liu, Porous bone tissue scaffold concept based on shape memory PLA/Fe3O4, Compos. Sci. Technol. 203 (2021) 108563, https://doi.org/10.1016/j.compscitech.2020.108563.

[8] Y. Zhang, J. Hu, R. Xie, Y. Yang, J. Cao, Y. Tu, Y. Zhang, T. Qin, X. Zhao, A programmable, fast-fixing, osteo-regenerative, biomechanically robust bone screw, Acta Biomater. 103 (2020) 293–305, https://doi.org/10.1016/j.actbio.2019.12.017.

[9] S. Bai, X. Zhang, X. Lv, M. Zhang, X. Huang, Y. Shi, C. Lu, J. Song, H. Yang, Bioinspired mineral–organic bone adhesives for stable fracture fixation and accelerated bone regeneration, Adv. Funct. Mater. 30 (5) (2020) 1908381, https://doi.org/10.1002/adfm.201908381.

[10] J. Yang, H. Qin, Y. Chai, P. zhang, Y. Chen, K. Yang, M. Qin, Y. Zhang, H. Xia, L. Ren, B. Yu, Molecular mechanisms of osteogenesis and antibacterial activity of Cu-bearing Ti alloy in a bone defect model with infection in vivo, Journal of Orthopaedic Translation 27 (2021) 77–89, https://doi.org/10.1016/j.jot.2020.10.004.

[11] G.-S. Shi, Y.-Y. Li, Y.-P. Luo, J.-F. Jin, Y.-X. Sun, L.-Z. Zheng, Y.-X. Lai, L. Li, G.-h. Fu, L. Qin, S.-H. Chen, Bioactive PLGA/tricalcium phosphate scaffolds incorporating phytomolecule icaritin developed for calvarial defect repair in rat model, Journal of Orthopaedic Translation 24 (2020) 112–120, https://doi.org/10.1016/j.jot.2020.05.008.

[12] J. Pan, T. Shirota, K. Ohno, K.-i. Michi, Effect of ovariectomy on bone remodeling adjacent to hydroxyapatite-coated implants in the tibia of mature rats, J. Oral Maxillofac. Surg. 58 (8) (2000) 877–882, https://doi.org/10.1053/joms.2000.8212.

[13] R. Agarwal, C. González-García, B. Torstrick, R.E. Guldberg, M. Salmerón-Sánchez, A.J. García, Simple coating with fibronectin fragment enhances stainless steel screw osseointegration in healthy and osteoporotic rats, Biomaterials 63 (2015) 137–145, https://doi.org/10.1016/j.biomaterials.2015.06.025.

[14] E. Neovius, T. Engstrand, Craniofacial reconstruction with bone and biomaterials: review over the last 11 years, J. Plast. Reconstr. Aesthetic Surg. 63 (10) (2010) 1615–1623, https://doi.org/10.1016/j.bjps.2009.06.003.

[15] L. Wang, Y. Qiu, Y. Guo, Y. Si, L. Liu, J. Cao, J. Yu, X. Li, Q. Zhang, B. Ding, Smart, elastic, and nanofiber-based 3D scaffolds with self-deploying capability for osteoporotic bone regeneration, Nano Lett. 19 (12) (2019) 9112–9120, https://doi.org/10.1021/acs.nanolett.9b04313.

[16] A.E. Jakus, A.L. Rutz, S.W. Jordan, A. Kannan, S.M. Mitchell, C. Yun, K.D. Koube, S. C. Yoo, H.E. Whiteley, C.-P. Richter, Hyperelastic "bone": a highly versatile, growth factor–free, osteoregenerative, scalable, and surgically friendly biomaterial, Sci. Transl. Med. 8 (358) (2016), https://doi.org/10.1126/scitranslmed.aaf7704, 358ra127-358ra127.

[17] Y. Xia, Y. He, F. Zhang, Y. Liu, J. Leng, A review of shape memory polymers and composites: mechanisms, materials, and applications, Adv. Mater. 33 (6) (2021) 2000713, https://doi.org/10.1002/adma.202000713.

[18] A. Lendlein, M. Balk, N.A. Tarazona, O.E. Gould, Bioperspectives for shape-memory polymers as shape programmable, active materials, Biomacromolecules 20 (10) (2019) 3627–3640, https://doi.org/10.1021/acs.biomac.9b01074.

[19] W. Zhao, L. Liu, F. Zhang, J. Leng, Y. Liu, Shape memory polymers and their composites in biomedical applications, Mater. Sci. Eng. C 97 (2019) 864–883, https://doi.org/10.1016/j.msec.2018.12.054.

[20] J.C. Worch, A.C. Weems, J. Yu, M.C. Arno, T.R. Wilks, R.T. Huckstepp, R. K. O'Reilly, M.L. Becker, A.P. Dove, Elastomeric polyamide biomaterials with stereochemically tuneable mechanical properties and shape memory, Nat. Commun. 11 (1) (2020) 1–11, https://doi.org/10.1038/s41467-020-16945-8.

[21] J. Wang, X. Li, Y. Song, Q. Su, X. Xiaohalati, W. Yang, L. Xu, B. Cai, G. Wang, Z. Wang, L. Wang, Injectable silk sericin scaffolds with programmable shape-memory property and neuro-differentiation-promoting activity for individualized brain repair of severe ischemic stroke, Bioactive Materials 6 (7) (2021) 1988–1999, https://doi.org/10.1016/j.bioactmat.2020.12.017.

[22] J. Xu, J. Song, High performance shape memory polymer networks based on rigid nanoparticle cores, Proc. Natl. Acad. Sci. Unit. States Am. 107 (17) (2010) 7652–7657, https://doi.org/10.1073/pnas.0912481107.

[23] P. Miaudet, A. Derre, M. Maugey, C. Zakri, P.M. Piccione, R. Inoubli, P. Poulin, Shape and temperature memory of nanocomposites with broadened glass transition, Science 318 (5854) (2007) 1294–1296, https://doi.org/10.1126/science.1145593.

[24] A. Lendlein, H. Jiang, O. Jünger, R. Langer, Light-induced shape-memory polymers, Nature 434 (7035) (2005) 879–882, https://doi.org/10.1038/nature03496.

[25] S. Ji, F. Fan, C. Sun, Y. Yu, H. Xu, Visible light-induced plasticity of shape memory polymers, ACS Appl. Mater. Interfaces 9 (38) (2017) 33169–33175, https://doi.org/10.1021/acsami.7b11188.

[26] L. Cera, G.M. Gonzalez, Q. Liu, S. Choi, C.O. Chantre, J. Lee, R. Gabardi, M.C. Choi, K. Shin, K.K. Parker, A bioinspired and hierarchically structured shape-memory material, Nat. Mater. 20 (2) (2021) 242–249, https://doi.org/10.1038/s41563-020-0789-2.

[27] S. Chen, F. Mo, F.J. Stadler, S. Chen, Z. Ge, H. Zhuo, Development of zwitterionic copolymers with multi-shape memory effects and moisture-sensitive shape memory effects, J. Mater. Chem. B 3 (32) (2015) 6645–6655, https://doi.org/10.1039/C5TB01075F.

[28] T. Chen, M. Pauly, P.M. Reis, A reprogrammable mechanical metamaterial with stable memory, Nature 589 (7842) (2021) 386–390, https://doi.org/10.1038/s41586-020-03123-5.

[29] M. Behl, M.Y. Razzaq, A. Lendlein, Multifunctional shape-memory polymers, Adv. Mater. 22 (31) (2010) 3388–3410, https://doi.org/10.1002/adma.200904447.

[30] Y. Li, A. Savan, A. Kostka, H. Stein, A. Ludwig, Accelerated atomic-scale exploration of phase evolution in compositionally complex materials, Materials Horizons 5 (1) (2018) 86–92, https://doi.org/10.1039/C7MH00486A.

[31] S. Park, N. Baugh, H.K. Shah, D.P. Parekh, I.D. Joshipura, M.D. Dickey, Ultrastretchable elastic shape memory fibers with electrical conductivity, Adv. Sci. 6 (21) (2019) 1901579, https://doi.org/10.1002/advs.201901579.
[32] Y.F. Zhang, N. Zhang, H. Hingorani, N. Ding, D. Wang, C. Yuan, B. Zhang, G. Gu, Q. Ge, Fast-response, stiffness-tunable soft actuator by hybrid multimaterial 3D printing, Adv. Funct. Mater. 29 (15) (2019) 1806698, https://doi.org/10.1002/adfm.201806698.
[33] Q. Zhao, J. Wang, H. Cui, H. Chen, Y. Wang, X. Du, Programmed shape-morphing scaffolds enabling facile 3D endothelialization, Adv. Funct. Mater. 28 (29) (2018) 1801027, https://doi.org/10.1002/adfm.201801027.
[34] M. Montgomery, S. Ahadian, L.D. Huyer, M.L. Rito, R.A. Civitarese, R. D. Vanderlaan, J. Wu, L.A. Reis, A. Momen, S. Akbari, Flexible shape-memory scaffold for minimally invasive delivery of functional tissues, Nat. Mater. 16 (10) (2017) 1038–1046, https://doi.org/10.1038/nmat4956.
[35] S. Zhu, J. Hu, Y. Zhang, A single polymer artificial muscle having dual-mode contractibility, temperature sensibility, and trainability through enthalpy change, Advanced Materials Technologies 4 (5) (2019) 1900017, https://doi.org/10.1002/admt.201900017.
[36] Y. Zhang, J. Hu, S. Zhu, T. Qin, F. Ji, A "trampoline" nanocomposite: tuning the interlayer spacing in graphene oxide/polyurethane to achieve coalesced mechanical and memory properties, Compos. Sci. Technol. 180 (2019) 14–22, https://doi.org/10.1016/j.compscitech.2019.04.033.
[37] D. Zhang, O.J. George, K.M. Petersen, A.C. Jimenez-Vergara, M.S. Hahn, M. A. Grunlan, A bioactive "self-fitting" shape memory polymer scaffold with potential to treat cranio-maxillo facial bone defects, Acta Biomater. 10 (11) (2014) 4597–4605, https://doi.org/10.1016/j.actbio.2014.07.020.
[38] Y. Liu, B. Shaw, M.D. Dickey, J. Genzer. Sequential self-folding of polymer sheets, Sci. Adv. 3 (3) (2017), e1602417, https://doi.org/10.1126/sciadv.1602417.
[39] R. Weissleder, A clearer vision for in vivo imaging, Nat. Biotechnol. 19 (4) (2001) 316–317, https://doi.org/10.1038/86684.
[40] A. Toncheva, P. Khelifa, Y. Paint, M. Voue, P. Lambert, P. Dubois, J.-M. Raquez, Fast IR-actuated shape-memory polymers using in situ silver nanoparticle-grafted cellulose nanocrystals, ACS Appl. Mater. Interfaces 10 (35) (2018) 29933–29942, https://doi.org/10.1021/acsami.8b10159.
[41] J. Shao, C. Ruan, H. Xie, P.K. Chu, X.F. Yu, Photochemical activity of black phosphorus for near-infrared light controlled in situ biomineralization, Adv. Sci. 7 (14) (2020) 2000439, https://doi.org/10.1002/advs.202000439.
[42] Z. Hu, S. Fu, A. Tang, Fabrication of light-triggered AuNP/CNC/SMP nano-composites, Bioresources 12 (1) (2017) 1982–1990, https://doi.org/10.15376/biores.12.1.1982-1990.
[43] X. Su, H. Li, X. Lai, Z. Chen, X. Zeng, 3D porous superhydrophobic CNT/EVA composites for recoverable shape reconfiguration and underwater vibration detection, Adv. Funct. Mater. 29 (24) (2019) 1900554, https://doi.org/10.1002/adfm.201900554.
[44] H. Xie, J. Shao, Y. Ma, J. Wang, H. Huang, N. Yang, H. Wang, C. Ruan, Y. Luo, Q.-Q. Wang, Biodegradable near-infrared-photoresponsive shape memory implants based on black phosphorus nanofillers, Biomaterials 164 (2018) 11–21, https://doi.org/10.1016/j.biomaterials.2018.02.040.
[45] A. Brown, S. Zaky, H. Ray, C. Sfeir, Porous magnesium/PLGA composite scaffolds for enhanced bone regeneration following tooth extraction, Acta Biomater. 11 (2015) 543–553, https://doi.org/10.1016/j.actbio.2014.09.008.
[46] S.C. Cifuentes, E. Frutos, J.L. González-Carrasco, M. Muñoz, M. Multigner, J. Chao, R. Benavente, M. Lieblich, Novel PLLA/magnesium composite for orthopedic applications: a proof of concept, Mater. Lett. 74 (2012) 239–242, https://doi.org/10.1016/j.matlet.2012.01.134.
[47] Y. Lai, Y. Li, H. Cao, J. Long, X. Wang, L. Li, C. Li, Q. Jia, B. Teng, T. Tang, J. Peng, D. Eglin, M. Alini, D.W. Grijpma, G. Richards, L. Qin, Osteogenic magnesium incorporated into PLGA/TCP porous scaffold by 3D printing for repairing challenging bone defect, Biomaterials 197 (2019) 207–219, https://doi.org/10.1016/j.biomaterials.2019.01.013.
[48] J. Long, B. Teng, W. Zhang, L. Li, M. Zhang, Y. Chen, Z. Yao, X. Meng, X. Wang, L. Qin, Preclinical evaluation of acute systemic toxicity of magnesium incorporated poly (lactic-co-glycolic acid) porous scaffolds by three-dimensional printing, Biomaterials Translational 2 (3) (2021) 272, https://doi.org/10.12336/biomatertransl.2021.03.009.
[49] P. Cheng, P. Han, C. Zhao, S. Zhang, H. Wu, J. Ni, P. Hou, Y. Zhang, J. Liu, H. Xu, S. Liu, X. Zhang, Y. Zheng, Y. Chai, High-purity magnesium interference screws promote fibrocartilaginous entheses regeneration in the anterior cruciate ligament reconstruction rabbit model via accumulation of BMP-2 and VEGF, Biomaterials 81 (2016) 14–26, https://doi.org/10.1016/j.biomaterials.2015.12.005.
[50] B. Li, P. Gao, H. Zhang, Z. Guo, Y. Zheng, Y. Han, Osteoimmunomodulation, osseointegration, and in vivo mechanical integrity of pure Mg coated with HA nanorod/pore-sealed MgO bilayer, Biomater Sci 6 (12) (2018) 3202–3218, https://doi.org/10.1039/c8bm00901e.
[51] X.N. Gu, X.H. Xie, N. Li, Y.F. Zheng, L. Qin, In vitro and in vivo studies on a Mg-Sr binary alloy system developed as a new kind of biodegradable metal, Acta Biomater. 8 (6) (2012) 2360–2374, https://doi.org/10.1016/j.actbio.2012.02.018.
[52] J.L. Wang, J.K. Xu, C. Hopkins, D.H. Chow, L. Qin, Biodegradable magnesium-based implants in orthopedics-A general review and perspectives, Adv. Sci. 7 (8) (2020) 1902443, https://doi.org/10.1002/advs.201902443.
[53] W. Yu, R. Li, J. Long, P. Chen, A. Hou, L. Li, X. Sun, G. Zheng, H. Meng, Y. Wang, A. Wang, X. Sui, Q. Guo, S. Tao, J. Peng, L. Qin, S. Lu, Y. Lai, Use of a three-dimensional printed polylactide-coglycolide/tricalcium phosphate composite scaffold incorporating magnesium powder to enhance bone defect repair in rabbits, J Orthop Translat 16 (2019) 62–70, https://doi.org/10.1016/j.jot.2018.07.007.
[54] X. Jing, Q. Ding, Q. Wu, W. Su, K. Yu, Y. Su, B. Ye, Q. Gao, T. Sun, X. Guo, Magnesium-based materials in orthopaedics: material properties and animal models, Biomaterials Translational 2 (3) (2021) 197, https://doi.org/10.12336/biomatertransl.2021.03.004.
[55] Y. Zhang, J. Xu, Y.C. Ruan, M.K. Yu, M. O'Laughlin, H. Wise, D. Chen, L. Tian, D. Shi, J. Wang, Implant-derived magnesium induces local neuronal production of CGRP to improve bone-fracture healing in rats, Nat. Med. 22 (10) (2016) 1160–1169, https://doi.org/10.1038/nm.4162.
[56] C. Li, J. Sun, K. Shi, J. Long, L. Li, Y. Lai, L. Qin, Preparation and evaluation of osteogenic nano-MgO/PMMA bone cement for bone healing in a rat critical size calvarial defect, J. Mater. Chem. B 8 (21) (2020) 4575–4586, https://doi.org/10.1039/D0TB00074D.
[57] S. Lin, G. Yang, F. Jiang, M. Zhou, S. Yin, Y. Tang, T. Tang, Z. Zhang, W. Zhang, X. Jiang, A magnesium-enriched 3D culture system that mimics the bone development microenvironment for vascularized bone regeneration, Adv. Sci. 6 (12) (2019) 1900209, https://doi.org/10.1002/advs.201900209.
[58] J. Long, W. Zhang, Y. Chen, B. Teng, B. Liu, H. Li, Z. Yao, D. Wang, L. Li, X.-F. Yu, Multifunctional magnesium incorporated scaffolds by 3D-Printing for comprehensive postsurgical management of osteosarcoma, Biomaterials (2021) 120950, https://doi.org/10.1016/j.biomaterials.2021.120950.
[59] G. Qiu, W. Ding, W. Tian, L. Qin, Y. Zhao, L. Zhang, J. Lu, D. Chen, G. Yuan, C. Wu, Medical additive manufacturing: from a frontier technology to the Research and development of products, Engineering 6 (2020) 1217–1221, https://doi.org/10.1016/j.eng.2020.10.002.
[60] R. Du, Y.-X. Su, Y. Yan, W.S. Choi, W.-F. Yang, C. Zhang, X. Chen, J.P. Curtin, J. Ouyang, B. Zhang, A systematic approach for making 3D-printed patient-specific implants for craniomaxillofacial reconstruction, Engineering 6 (11) (2020) 1291–1301, https://doi.org/10.1016/j.eng.2020.02.019.
[61] Y. Wang, Q. Tan, F. Pu, D. Boone, M. Zhang, A review of the application of additive manufacturing in prosthetic and orthotic clinics from a biomechanical perspective, Engineering (2020), https://doi.org/10.1016/j.eng.2020.07.019.
[62] L. Qin, D. Yao, L. Zheng, W.-C. Liu, Z. Liu, M. Lei, L. Huang, X. Xie, X. Wang, Y. Chen, X. Yao, J. Peng, H. Gong, J.F. Griffith, Y. Huang, Y. Zheng, J.Q. Feng, Y. Liu, S. Chen, D. Xiao, D. Wang, J. Xiong, D. Pei, P. Zhang, X. Pan, X. Wang, K.-M. Lee, C.-Y. Cheng, Phytomolecule icaritin incorporated PLGA/TCP scaffold for steroid-associated osteonecrosis: proof-of-concept for prevention of hip joint collapse in bipedal emus and mechanistic study in quadrupedal rabbits, Biomaterials 59 (2015) 125–143, https://doi.org/10.1016/j.biomaterials.2015.04.038.
[63] Y. Lai, H. Cao, X. Wang, S. Chen, M. Zhang, N. Wang, Z. Yao, Y. Dai, X. Xie, P. Zhang, X. Yao, L. Qin, Porous composite scaffold incorporating osteogenic phytomolecule icariin for promoting skeletal regeneration in challenging osteonecrotic bone in rabbits, Biomaterials 153 (2018) 1–13, https://doi.org/10.1016/j.biomaterials.2017.10.025.
[64] Y. Lai, L. Li, S. Chen, M. Zhang, X. Wang, P. Zhang, L. Qin, A Novel magnesium composed PLGA/TCP porous scaffold fabricated by 3D printing for bone regeneration, Journal of Orthopaedic Translation 2 (4) (2014) 218–219, https://doi.org/10.1016/j.jot.2014.07.025.
[65] Y. Lai, H. Cao, X. Wang, S. Chen, M. Zhang, N. Wang, Z. Yao, Y. Dai, X. Xie, P. Zhang, Porous composite scaffold incorporating osteogenic phytomolecule icariin for promoting skeletal regeneration in challenging osteonecrotic bone in rabbits, Biomaterials 153 (2018) 1–13, https://doi.org/10.1016/j.biomaterials.2017.10.025.
[66] Y. Wang, W. Cui, X. Zhao, S. Wen, Y. Sun, J. Han, H. Zhang, Bone remodeling-inspired dual delivery electrospun nanofibers for promoting bone regeneration, Nanoscale 11 (1) (2019) 60–71, https://doi.org/10.1039/C8NR07329E.
[67] P.P. Spicer, J.D. Kretlow, S. Young, J.A. Jansen, F.K. Kasper, A.G. Mikos, Evaluation of bone regeneration using the rat critical size calvarial defect, Nat. Protoc. 7 (10) (2012) 1918–1929, https://doi.org/10.1038/nprot.2012.113.
[68] E. Kitamura, R. Stegaroiu, S. Nomura, O. Miyakawa, Biomechanical aspects of marginal bone resorption around osseointegrated implants: considerations based on a three-dimensional finite element analysis, Clin. Oral Implants Res. 15 (4) (2004) 401–412, https://doi.org/10.1111/j.1600-0501.2004.01022.x.
[69] X. Zhao, S. Liu, L. Yildirimer, H. Zhao, R. Ding, H. Wang, W. Cui, D. Weitz, Injectable stem cell-laden photocrosslinkable microspheres fabricated using microfluidics for rapid generation of osteogenic tissue constructs, Adv. Funct. Mater. 26 (17) (2016) 2809–2819, https://doi.org/10.1002/adfm.201504943.
[70] Y. Lai, Y. Li, H. Cao, J. Long, X. Wang, L. Li, C. Li, Q. Jia, B. Teng, T. Tang, Osteogenic magnesium incorporated into PLGA/TCP porous scaffold by 3D printing for repairing challenging bone defect, Biomaterials 197 (2019) 207–219, https://doi.org/10.1016/j.biomaterials.2019.01.013.
[71] A. Nedoseka, 2 - welding stresses and strains, in: A. Nedoseka (Ed.), Fundamentals of Evaluation and Diagnostics of Welded Structures, Woodhead Publishing2012, pp. 72-182.
[72] F. Lu, B. Song, P. He, Z. Wang, J. Wang, Electrochemical impedance spectroscopy (EIS) study on the degradation of acrylic polyurethane coatings, RSC Adv. 7 (23) (2017) 13742–13748, https://doi.org/10.1039/C6RA26341K.
[73] M. Rashad, F. Pan, A. Tang, M. Asif, J. She, J. Gou, J. Mao, H. Hu, Development of magnesium-graphene nanoplatelets composite, J. Compos. Mater. 49 (3) (2015) 285–293, https://doi.org/10.1177/0021998313518360.
[74] N.-C. Weng, C.-F. Wu, W.-C. Tsen, C.-L. Wu, M.-C. Suen, Synthesis and properties of shape memory polyurethanes generated from schiff-base chain extender containing benzoyl and pyridyl rings, Des. Monomers Polym. 21 (1) (2018) 55–63, https://doi.org/10.1080/15685551.2018.1450467.
[75] A. Shaabani, R. Sedghi, H. Motasadizadeh, R. Dinarvand, Self-healable conductive polyurethane with the body temperature-responsive shape memory for bone tissue

engineering, Chem. Eng. J. 411 (2021) 128449, https://doi.org/10.1016/j.cej.2021.128449.
[76] H. Xie, J. Shao, Y. Ma, J. Wang, H. Huang, N. Yang, H. Wang, C. Ruan, Y. Luo, Q.-Q. Wang, P.K. Chu, X.-F. Yu, Biodegradable near-infrared-photoresponsive shape memory implants based on black phosphorus nanofillers, Biomaterials 164 (2018) 11–21, https://doi.org/10.1016/j.biomaterials.2018.02.040.
[77] J. Wang, F. Witte, T. Xi, Y. Zheng, K. Yang, Y. Yang, D. Zhao, J. Meng, Y. Li, W. Li, Recommendation for modifying current cytotoxicity testing standards for biodegradable magnesium-based materials, Acta Biomater. 21 (2015) 237–249, https://doi.org/10.1016/j.actbio.2015.04.011.
[78] S. Yoshizawa, A. Brown, A. Barchowsky, C. Sfeir, Magnesium ion stimulation of bone marrow stromal cells enhances osteogenic activity, simulating the effect of magnesium alloy degradation, Acta Biomater. 10 (6) (2014) 2834–2842, https://doi.org/10.1016/j.actbio.2014.02.002.